

## A synthetic sample of short-cadence solar-like oscillators for TESS

WARRICK H. BALL,<sup>1,2</sup> WILLIAM J. CHAPLIN,<sup>1,2</sup> MATHEW SCHOFIELD,<sup>1,2</sup> ANDREA MIGLIO,<sup>1,2</sup> DIEGO BOSSINI,<sup>3</sup>  
GUY R. DAVIES,<sup>1,2</sup> AND LÉO GIRARDI<sup>3</sup>

<sup>1</sup>*School of Physics and Astronomy, University of Birmingham, Edgbaston, Birmingham B15 2TT, United Kingdom*

<sup>2</sup>*Stellar Astrophysics Centre, Department of Physics and Astronomy, Aarhus University, Ny Munkegade 120, DK-8000 Aarhus C, Denmark*

<sup>3</sup>*INAF-Osservatorio Astronomico di Padova, Vicolo dell'Osservatorio 5, I-35122 Padova, Italy*

### ABSTRACT

NASA's *Transiting Exoplanet Survey Satellite* (TESS) has begun a two-year survey of most of the sky, which will include lightcurves for thousands of solar-like oscillators sampled at a cadence of two minutes. To prepare for this steady stream of data, we present a mock catalogue of lightcurves, designed to realistically mimic the properties of the TESS sample. In the process, we also present the first public release of the asteroFLAG Artificial Dataset Generator, which simulates lightcurves of solar-like oscillators based on input mode properties. The targets are drawn from a simulation of the Milky Way's populations and are selected in the same way as TESS's true Asteroseismic Target List. The lightcurves are produced by combining stellar models, pulsation calculations and semi-empirical models of solar-like oscillators. We describe the details of the catalogue and provide several examples. Though white noise is the only source of noise in the lightcurves we provide, other sources can be added easily. This mock catalogue will be valuable in testing asteroseismology pipelines for TESS and our methods can be applied in preparation and planning for other observatories and observing campaigns.

*Keywords:* stars: oscillations (including pulsations)

### 1. INTRODUCTION

The study of stellar oscillations—*asteroseismology*—has undergone a revolution, driven by space-based photometric observations from COROT (Auvergne et al. 2009), *Kepler* (Borucki et al. 2010) and K2 (Howell et al. 2014). In particular, space-based photometry has provided data of unprecedented quality for solar-like oscillators, whose low-amplitude oscillations had previously been notoriously difficult to observe.

NASA's *Transiting Exoplanet Survey Satellite* (TESS, Ricker et al. 2015) will extend this new era. Like *Kepler*, TESS is chiefly an exoplanet survey mission but its continuous, high-cadence observations are also suited to the study of stellar oscillations. TESS will observe most of the sky in roughly month-long sectors covering four  $24^\circ \times 24^\circ$  areas from the ecliptic poles to near the ecliptic plane. The mission will produce full-frame images (FFIs) every 30 minutes as well as light curves for a selection of targets sampled at a short cadence of two minutes, which is necessary for the seismology of cool main-sequence and

subgiant stars. Once reduced to lightcurves, the FFIs will also allow asteroseismic analysis but here we restrict our attention to short-cadence targets. The initial data will be released after about six months of operations, after which new data will be released roughly monthly. Each month of short-cadence data is expected to include hundreds of stars in which solar-like oscillations will be detected.

In preparation for this rapid flow of data, we present here a mock catalogue of TESS lightcurves for a realistically-selected sample of solar-like oscillators observed at short cadence. These will be used to test parameter extraction pipelines (and potentially model-fitting pipelines) with known physical parameters. Although some important quantities (e.g. rotation rates) cannot currently be predicted a priori, the rich phenomenology of solar-like oscillators derived from previous missions allows us to generate realistic lightcurves using empirical methods. These lightcurves are also provided in a simple format so that they can be supplemented with other signals, like transiting planets or systematic effects.

We start by presenting our method for producing stellar models for a sample that mimics the Asteroseismic Target List (ATL, Schofield et al., in prep.) of the TESS

Asteroseismic Science Consortium (TASC, Section 2). This is followed by the inputs and methods by which we computed lightcurves for each star in that sample (Section 3). We then describe the structure of our model catalogue and present several example results (Section 4) before discussing shortcomings and potential future applications of our methods (Section 5) and concluding (Section 6).

## 2. METHODS

### 2.1. Stellar models

All of the stellar models used in this work were computed using Modules for Experiments in Stellar Astrophysics<sup>1</sup> (MESA), revision 7385 (Paxton et al. 2011, 2013). The stellar model grids used in the Galaxy simulation (see Sec. 2.2) are the same as described by Rodrigues et al. (2017) and the same inputs were used to recreate individual stellar model profiles at the interpolated parameter values (see Sec. 2.4). Full details are given by Rodrigues et al. (2017) but we give the main parameters again here.

The models use the solar metal mixture of Grevesse & Noels (1993), with solar metal and helium abundances  $Z_{\odot} = 0.01756$  and  $Y_{\odot} = 0.26618$ . Stellar models at other metallicities follow the enrichment law  $Y = 0.2485 + 1.007 \times Z$ . The atmospheric model is that of Krishna Swamy (1966), which gives a solar-calibrated mixing length parameter  $\alpha_{\text{MLT}} = 1.9657$ . Opacities are taken from the OPAL tables (Iglesias & Rogers 1996) at high temperatures ( $\log_{10}(T/\text{K}) \geq 4.1$ ), Ferguson et al. (2005) at low temperatures ( $\log_{10}(T/\text{K}) \leq 4.0$ ) and blended linearly between ( $4.0 \leq \log_{10}(T/\text{K}) \leq 4.1$ ). The equation of state is the MESA default, which is derived from the OPAL equation of state Rogers & Nayfonov (2002) in the region relevant for our stellar models.

### 2.2. Galaxy simulation

We simulated the population of stars in the Milky Way using TRILEGAL (Girardi et al. 2005). The simulation used the default parameters described by Girardi et al. (2012), which comprise a thin disc, thick disc, halo and bulge. The simulation includes a rough model for extinction, in which the total extinction determined by Schlegel et al. (1998) is assumed to be caused by an exponential dust disc with a scale height of 110 pc. Bolometric corrections and extinction coefficients were calculated for the TESS bandpass in a Vega magnitude system. The stellar models (as described in the previous section) span masses from  $0.60$  to  $2.50 M_{\odot}$  in steps of between  $0.05$

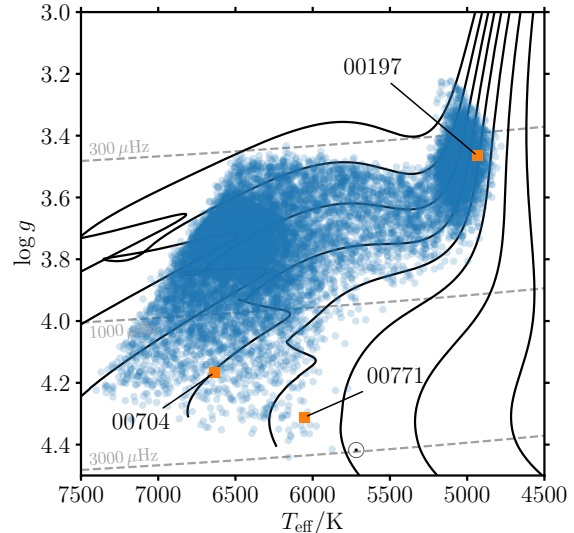


**Figure 1.** Kiel diagram of the stars selected by the ATL code from the TRILEGAL simulation. The solid black lines are evolutionary tracks at solar metallicity for masses from  $0.6 M_{\odot}$  to  $2.0 M_{\odot}$  in steps of  $0.2 M_{\odot}$ . Orange points are stars whose power spectra are shown elsewhere. Star 00197 appears in Figs 3 and 4, star 00704 in Fig. 5 and star 00771 in Fig. 6. The dashed grey lines, from top to bottom, show constant  $\nu_{\text{max}} = 300, 1000$  and  $3000 \mu\text{Hz}$ .

and  $0.20 M_{\odot}$  (see Table 1 of Rodrigues et al. 2017) and metallicities  $[\text{Fe}/\text{H}]$  from  $-1.00$  to  $0.50$  in steps of  $0.25$ . The limits of the stellar model grid naturally restrict our base population to those ranges. The population was selected to cover the whole sky down to a magnitude limit of  $12.5$  in the TESS bandpass.

### 2.3. Target selection

We ranked the stars in the TRILEGAL simulation by the likelihood of detecting solar-like oscillations, as determined by the same code used to produce the Asteroseismic Target List (ATL, Schofield et al., in prep.) for Working Groups 1 and 2 of the TESS Asteroseismic Science Consortium (TASC). The code is described by Campante et al. (2016) and determines the detection probability by the same method as Chaplin et al. (2011), appropriately modified for TESS using its expected noise characteristics (Sullivan et al. 2015). In addition, we used the distance moduli provided by the TRILEGAL simulation, rather than also creating mock distances to mimic the Tycho–Gaia Astrometric Solution (TGAS, as used in Campante et al. 2016) or Gaia DR2 (which is being used for the final version of the ATL).

TESS’s observing strategy is important because it divides the sky into 26 partially-overlapping observing sectors of varying durations. We shall partially classify

<sup>1</sup> <http://mesa.sourceforge.net>

our results by these sectors. The satellite observes each hemisphere of the sky in sectors containing four  $24^\circ \times 24^\circ$  areas that cover a strip of the sky from the ecliptic pole to near the ecliptic plane. Each hemisphere is observed for 13 sectors and each sector is observed for about 27.4 days on average. After observing in one hemisphere, the satellite will re-orient to observe the other hemisphere. The first sector is centred on a galactic longitude of  $315.8^\circ$ , which we have replicated in our mock sample.

TESS uses an orbit in 2:1 resonance with the moon, in which the lengths of the orbits vary within a range of a few days (Dichmann et al. 2014, 2016). The details of the pointings depend on the precise orientation of the spacecraft and these are not known until the observations of a given sector begin. In our mock sample, we have extrapolated approximate pointings and sector durations from perigee data provided by the TESS team.<sup>2</sup> For the sector pointings, we fit the times (as Julian dates) of the mid-sector perigees  $t_{\text{perigee}}$  with the formula

$$t_{\text{perigee}} = 2458339.922 + 27.266(n - 1) + 2.386 \sin(2\pi(0.0937(n - 1) - 0.0683)) \quad (1)$$

where  $n$  is the sector number, from 1 to 26. We then took the pointing of a given sector to be the anti-solar direction at that time. For the sector durations  $\Delta t$ , we fit a similar formula to the durations between perigees at the start and end of each sector,

$$\Delta t/d = 27.276 + 1.493 \sin(2\pi(0.00345t + 0.171)) \quad (3)$$

where  $t$  is the Julian date at the start of a sector. Though not perfectly accurate, these formulae give our mock sample a realistic variation in the durations and pointings of each sector all the way to the end of the nominal mission.

Running the ATL code on our TRILEGAL simulation data provided a ranking for all the stars in the simulation. To create our mock sample, we selected enough stars for each sector to contain at least 1000 stars. The mock sample contains 12731 stars and each sector contains between 1000 and 1263 targets (many of which appear in more than one sector). In the output ATL target list, 99.07 per cent of the stars are in the thin disc, 0.85 per cent in the thick disc, 0.08 per cent in the halo and none in the bulge. Fig. 1 shows the stars in the Kiel diagram (effective temperature  $T_{\text{eff}}$  versus surface gravity  $\log g$ ).

Note that the ATL target selection presumably contaminates the sample with some number of classical pulsators, in particular  $\gamma$  Doradus variables. Indeed,  $\gamma$

Doradus itself is one of the targets in the real ATL. This is a deliberate choice to better sample the transition from solar-like oscillations to coherent pulsations and to search for potential hybrid oscillators. We have assumed that all the ATL-selected stars are solar-like oscillators and have ignored this contamination. Using various estimates of the red edge of the  $\gamma$  Doradus instability strip (e.g. Dupret et al. 2004), we estimate that as much as 20 per cent of our sample might be in the instability strip. Most of these stars, however, are ranked in the lowest quarter of our sample.

The target selection also does not account for the binarity of systems, even though the TRILEGAL simulation does generate stars in binary systems. The ATL selects its targets using the single star data and therefore selects targets that might actually be difficult to observe because of a companion. For reference, TRILEGAL labels 64.0 per cent of the selected targets as single stars, 28.0 per cent as primaries and 8.0 per cent as secondaries.

#### 2.4. Stellar model parameters

The simulated population does not provide complete stellar models, which are required to compute mode frequencies, so we recomputed evolutionary tracks with the initial parameters in the TRILEGAL simulation and stored the final models of these tracks for the oscillation calculation. Because TRILEGAL interpolates in a grid of models to compute a star's observable properties, we expect some differences in stellar properties caused by interpolation. We initially proceeded naively, using exactly the stellar age given by the TRILEGAL data. This gave differences of up to about 5 per cent in  $T_{\text{eff}}$  and  $\log(L/L_\odot)$ .

To reduce the differences in these key properties, we instead evolved the star until the misfit in  $T_{\text{eff}}$  and  $\log(L/L_\odot)$  reached a minimum near the age given in the TRILEGAL data. This improved the mean accuracy to better than about 0.5 per cent at the cost of introducing small discrepancies in the ages, of up to about 1 per cent on average. Specifically, we minimised the misfit

$$\chi^2 = \left( \frac{T_{\text{eff,MESA}} - T_{\text{eff,TRI}}}{150 \text{ K}} \right)^2 \quad (4)$$

$$+ \left( \frac{\log_{10}(L_{\text{MESA}}/L_\odot) - \log_{10}(L_{\text{TRI}}/L_\odot)}{0.03} \right)^2 \quad (5)$$

where the subscripts MESA and TRI indicate quantities from the recomputed MESA model or the TRILEGAL data.

Like Rodrigues et al. (2017), we evolved our models starting from the pre-main-sequence. MESA sometimes fails to converge on initial models when using atmospheric  $T(\tau)$  relations so Rodrigues et al. (2017) used

<sup>2</sup> [https://figshare.com/articles/TESS\\_Perigee\\_Times/6875525](https://figshare.com/articles/TESS_Perigee_Times/6875525)

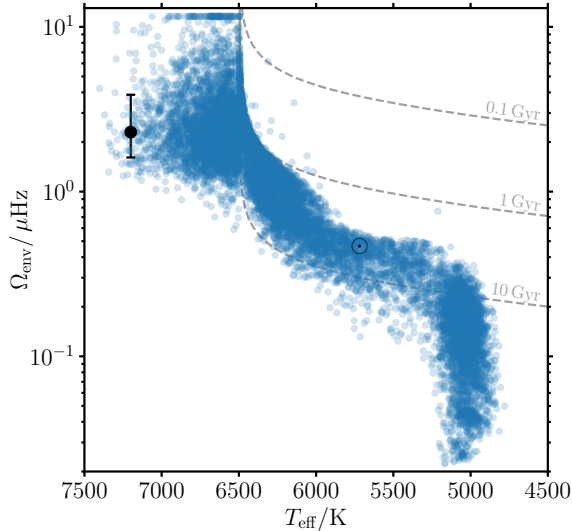


**Figure 2.** Envelope rotation rates for all the stars selected by the ATL code from the TRILEGAL simulation. The dashed grey lines are rotation rates for fixed ages, from top to bottom, 0.1 Gyr, 1 Gyr and 10 Gyr, evaluated using the formula for cool stars (eq. 6). The black point shows the median and standard deviation of the normal distribution (in period) used for stars hotter than about 6500 K.

different values of the initial central temperature  $T_c$  for different evolutionary tracks. When recomputing models at interpolated parameter values from the TRILEGAL output, we also interpolated  $T_c$  linearly as a function of mass  $M$  and metallicity  $Z$ . This still led to some runs failing to converge on an initial model. In these cases, we increased the initial central temperature by 1000 K at a time until an initial model converged and the run could proceed. About 4 per cent of all our models require this step, and just over half of those require just one change to  $T_c$ .

### 2.5. Rotation profiles

A priori modelling of stellar rotation rates is an unsolved problem. For example, stellar models broadly predict that the cores of low-mass red giants should rotate faster than asteroseismic inferences suggest (e.g. Eggenberger et al. 2012; Marques et al. 2013). Similarly, solar models incorporating rotation (e.g. Turck-Chièze et al. 2010) predict differential rotation in the Sun’s radiative zone, which is at odds with the helioseismic inference of solid-body rotation down to about  $0.2 R_\odot$  (Howe 2009) from the centre. In the absence of a reliable forward model of stellar rotation, we used empirical relations to predict the rotation rates of the stars in our sample.

For each star, we first compute a rotation rate predicted by the models of Angus et al. (2015) using the median values of their parameters. For stars with  $T_{\text{eff}} > 6500$  K, we use their formula for hot dwarfs (their eq. 7) and draw a rotation period  $P$  from a normal distribution with mean 5.0 d and standard deviation 2.1 d. For stars with  $T_{\text{eff}} < 6500$  K, we use their formula for cool dwarfs (their eq. 8)

$$P = 0.40(B - V - 0.45)^{0.31} t^{0.55} \quad (6)$$

where the colour  $B - V$  is determined from  $T_{\text{eff}}$  according to the fitting formula by Torres (2010). We do not use the subgiant formulae by Angus et al. (2015) because their subgiant sample has stars mostly hotter than about 6000 K and generally gives faster rotation rates than observed in low-luminosity red giants. Their model of subgiant rotation rates was principally introduced to avoid contaminating the gyrochronology relation for cool main-sequence stars. As a precaution, we set a minimum rotation period of 1 d (i.e. a maximum rotation frequency of  $11.57 \mu\text{Hz}$ ).

For stars on the main sequence (defined by a central hydrogen abundance  $X_c > 10^{-4}$ ), we assume that the star is rotating rigidly, so that the rotation rate is constant throughout the stellar model. Although results for radial differential rotation in main-sequence stars are limited, they are consistent with solid-body rotation (e.g. Benomar et al. 2015; Nielsen et al. 2015, 2017).

For stars that have depleted hydrogen in their cores, we divide the rotation rate from eq. 6 by  $(R/R_{\text{TAMS}})^2$ , where  $R_{\text{TAMS}}$  is the radius of the star at the end of the main sequence. This factor represents a naïve conservation of angular momentum as the star expands gives rotation rates that agree better with the envelope rotation rates found by Deheuvels et al. (2014) in six subgiants and low-luminosity red giants.

For these post-main-sequence stars, we also draw a core rotation rate from a normal distribution with mean  $0.375 \mu\text{Hz}$  and standard deviation  $0.105 \mu\text{Hz}$ , which is derived from those stars in the sample studied by Mosser et al. (2012a) with large frequency separations  $\Delta\nu > 12 \mu\text{Hz}$  (i.e. the spacing between modes of the same degree and consecutive radial order). If this new rotation rate is greater than the first one, then the lower rate is taken as rotation rate of the convective envelope ( $\Omega_{\text{env}}$ ) and the greater rate as the rotation rate of the convectively-stable core ( $\Omega_{\text{core}}$ ).

Fig. 2 shows the envelope rotation rates of all the stars selected by the ATL code from the TRILEGAL simulation.

### 2.6. Frequency calculation



For each stellar model, we used GYRE<sup>3</sup> (Townsend & Teitler 2013; Townsend et al. 2018) to compute adiabatic mode frequencies between 0.15 and 0.95 of the acoustic cut-off frequency for angular degrees  $\ell$  from 0 to 3. Specifically, for all the modes, we used a grid of 800 frequencies distributed linearly in frequency and, for the non-radial modes, we added extra grids of 1000, 3000 and 14000 frequencies for the  $\ell = 1, 2$  and 3 modes, distributed linearly in period. The latter grids recover mixed modes more efficiently, which most of our target have. The outer boundary condition matches the oscillations to the oscillations in an isothermal atmosphere, as implemented in the pulsation code ADIPLS (Christensen-Dalsgaard 2008).

Rotational splittings are computed under the assumptions that the rotation is slow, is purely a function of radius, and can be treated as a perturbation to the non-rotating mode frequencies. Under these assumptions, the rotational splitting for a mode of radial order  $n$ , angular degree  $\ell$  and azimuthal order  $m$  is

$$\delta\nu_{n\ell m} = m \frac{\int_0^R (\xi_r^2 + (\ell(\ell+1) - 1)\xi_h^2 - 2\xi_r\xi_h) r^2 \rho \Omega dr}{\int_0^R (\xi_r^2 + \ell(\ell+1)\xi_h^2) r^2 \rho dr} \quad (7)$$

where  $\xi_r$  and  $\xi_h$  are the radial and horizontal displacement eigenfunctions of the oscillation mode and  $\Omega$  is the rotation profile, which is given by

$$\Omega(r) = \begin{cases} \Omega_{\text{core}} & \text{if } r \leq r_{\text{BCZ}} \\ \Omega_{\text{env}} & \text{if } r > r_{\text{BCZ}} \end{cases} \quad (8)$$

Eq. 7 is usually written in the form

$$\delta\nu_{n\ell m} = m\beta_{n\ell} \int_0^R K_{n\ell} \Omega dr \quad (9)$$

where we have defined

$$K_{n\ell} = \frac{(\xi_r^2 + (\ell(\ell+1) - 1)\xi_h^2 - 2\xi_r\xi_h) r^2 \rho}{\int_0^R (\xi_r^2 + (\ell(\ell+1) - 1)\xi_h^2 - 2\xi_r\xi_h) r^2 \rho dr} \quad (10)$$

and

$$\beta_{n\ell} = \frac{\int_0^R (\xi_r^2 + (\ell(\ell+1) - 1)\xi_h^2 - 2\xi_r\xi_h) r^2 \rho}{\int_0^R (\xi_r^2 + \ell(\ell+1)\xi_h^2) r^2 \rho dr} \quad (11)$$

Using these definitions, a rotational splitting can be expressed as

$$\delta\nu_{n\ell} = m\beta_{n\ell} \left( \Omega_{\text{core}} \int_0^{r_{\text{BCZ}}} K_{n\ell} dr + \Omega_{\text{env}} \int_{r_{\text{BCZ}}}^R K_{n\ell} dr \right) \quad (12)$$

which is a weighted mean of the core and envelope rotation rates. Modes that are more sensitive to the core will have frequency splittings that are weighted more strongly towards the core rotation rate, and vice versa. For rigidly rotating stars (i.e.  $\Omega_{\text{core}} = \Omega_{\text{env}}$ ), eq. 12 simplifies further to

$$\delta\nu_{n\ell} = m\beta_{n\ell}\Omega_{\text{env}} \quad (13)$$

because the rotational kernels are defined to have unit integral.

Davies et al. (2014) demonstrated that a star's oscillation frequencies can be significantly Doppler-shifted by its line-of-sight velocity. To mimic this effect in our data, we generated line-of-sight velocities for our stars that mimic the observed radial velocities for nearby stars in Gaia's second data release (DR2, Katz et al. 2018). Specifically, we fit a second-order polynomial in  $\sin(l)$  to the mean and standard deviation of the radial velocities of stars with parallaxes greater than 0.833 mas. This gives the following simple functions of galactic longitude  $l$  for the median line-of-sight velocity  $v_r$  and its standard deviation  $\sigma_{v_r}$ :

$$\begin{aligned} v_r(l)/\text{km} \cdot \text{s}^{-1} &= 1.4 + 18.8 \sin(l + 207.7^\circ) \\ &\quad + 7.9 \sin(2l - 5.3^\circ) \\ \sigma_{v_r}(l)/\text{km} \cdot \text{s}^{-1} &= 30.0 - 1.1 \sin(l + 260.8^\circ) \\ &\quad + 4.3 \sin(2l + 70.6^\circ) \end{aligned}$$

For a star at a given galactic longitude  $l$ , we draw a random line-of-sight velocity from a normal distribution with mean  $v_r(l)$  and standard deviation  $\sigma_{v_r}(l)$  and multiply the raw frequencies by  $\sqrt{(1 - v_r/c)/(1 + v_r/c)}$ , where  $c$  is the speed of light.

We close this section by noting that we have not attempted to incorporate *surface effects*: the systematic difference between observed and modelled mode frequencies caused by poor modelling of the near-surface layers of solar-like oscillators. Several empirical corrections have been proposed (Kjeldsen et al. 2008; Ball & Gizon 2014; Sonoi et al. 2015) and several groups have computed frequencies for models that incorporate information from three-dimensional radiation hydrodynamics simulations (e.g. Sonoi et al. 2015; Ball et al. 2016; Jørgensen et al. 2017; Trampedach et al. 2017). Only a few results (e.g. Houdek et al. 2017; Sonoi et al. 2017) consider effects beyond the structural changes. None of these results, however, is able to predict the complete surface effect for given stellar parameters. As a result, we have elected not to add any surface effect rather than invent an empirical scheme based on the incomplete treatments available at this point.

### 3. LIGHTCURVE SIMULATIONS

<sup>3</sup> <https://bitbucket.org/rhdtownsend/gyre/>

### 3.1. Introduction

We computed artificial lightcurves using the asteroFLAG Artificial Dataset Generator, version 3 (AADG3). Variants of the code have been developed over many years and extensively used, particularly for validating the data analysis of ground-based radial velocity measurements of solar oscillations and stellar oscillations. The core of the code, which simulates stochastically-driven oscillations in the time domain, was presented by Chaplin et al. (1997). The Solar Fitting at Low Angular Degree Group (solarFLAG) used and developed the code to test their data-analysis packages in two hare-and-hounds exercises (Chaplin et al. 2006; Jiménez-Reyes et al. 2008). The code was further developed for the Asteroseismic Fitting at Low Angular Degree Group (asteroFLAG, e.g. Chaplin et al. 2008b) from which the current version is chiefly derived. Details of the code were most recently described by Howe et al. (2015). The version used here has been rewritten into Fortran 95 and we are now making it publicly available<sup>4</sup> under the GNU General Public License, version 3.<sup>5</sup>

The core component of AADG3 simulates the lightcurves for all modes with the same angular degree  $\ell$  and azimuthal order  $m$ . The code first generates an exponentially-damped random walk (equivalent to an AR(1) process) that is the same for all modes of the specified  $\ell$  and  $m$ . This is the *correlated* driving term, which we denote  $u_c$ , and is interpreted as the component of the granulation that contributes to exciting all modes of a given  $\ell$  and  $m$ . Then, for each radial order with the specified  $\ell$  and  $m$ , the code generates another exponentially-damped random walk, which is the *uncorrelated* driving term, denoted  $u_u$ . This represents the component of the granulation that only drives a single mode of a given  $n$ ,  $\ell$  and  $m$ . The two sequences are added to give an overall of driving term for that mode,

$$u = au_u + \sqrt{1 - a^2}u_c \quad (14)$$

where  $a$  is a user-provided parameter, which we set at 0.45. Toutain et al. (2006) introduced the correlated driving term to model the asymmetry in the mode profiles. The first 6 d of data are truncated from the beginning of the sequence to allow the damped random walk to relax into equilibrium.

To generate a complete lightcurve, AADG3 first generates the contribution of all overtones of a given  $\ell$  and  $m$  using the Laplace transform solution of a driven, damped harmonic oscillator (Chaplin et al. 1997) with a sequence

$u$  (eq. 14) as the driving term. The code repeats this for each combination of  $\ell$  and  $m$ . The final lightcurve is the combination of the lightcurves and driving terms for each  $\ell$  and  $m$ , weighted to reproduce the appropriate relative amplitudes (see Howe et al. 2015).

### 3.2. Mode lifetimes and linewidths

Solar-like oscillations are intrinsically damped by near-surface convection (which also excites them) and the oscillations therefore have finite lifetimes. In other words, the resonant peaks in the power spectrum, which are well-approximated by Lorentzian curves, have measurable linewidths (except for some very long-lived mixed modes in evolved solar-like oscillators). There are currently few theoretical predictions of the linewidths of solar-like oscillators (e.g. Houdek 2017; Aarslev et al. 2018) and even those cannot be routinely and rapidly computed for a large number of targets. We therefore use a semi-empirical description based on data from the nominal *Kepler* mission.

We parametrise the linewidths  $\Gamma$  as a function of frequency using the same formula as Appourchaux et al. (2014, eq. 1) and Lund et al. (2017, eq. 30):

$$\ln \Gamma = \alpha \ln(\nu/\nu_{\max}) + \ln \Gamma_\alpha + \left( \frac{\ln \Delta\Gamma_{\text{dip}}}{1 + \left( \frac{2 \ln(\nu/\nu_{\text{dip}})}{\ln(W_{\text{dip}}/\nu_{\max})} \right)^2} \right) \quad (15)$$

where  $\alpha$ ,  $\Gamma_\alpha$ ,  $\Delta\Gamma_{\text{dip}}$ ,  $\nu_{\text{dip}}$  and  $W_{\text{dip}}$  are all parameters that are simultaneously fit as bilinear functions of  $T_{\text{eff}}$  and  $\nu_{\max}$ . That is, each parameter  $x$  is expressed as

$$x = a_x + b_x T_{\text{eff}} + c_x \nu_{\max} \quad (16)$$

where  $a_x$ ,  $b_x$  and  $c_x$  are the free parameters, of which there are 15 in total (3 for each of the 5 parameters in eq. 16). We fit all 15 parameters at once, using fits to each LEGACY target (with all  $b_x$  and  $c_x = 0$ ) as initial guesses, to a sample containing all the radial mode frequencies reported in the LEGACY sample as well as the 25 red giants with highest  $\nu_{\max}$  in the sample studied by Davies et al. (2018, in prep.). Table 1 shows the best-fitting parameters found in this way.

The coupling of g- and p-modes in evolved stars affects the damping rates (see e.g. Basu & Chaplin 2017). We divide the linewidth from equation 15 by the ratio  $Q_{n\ell}$

$$Q_{n\ell} = \frac{\mathcal{I}_{n\ell}}{\mathcal{I}_0(\nu_{n\ell})} \quad (17)$$

where  $\nu_{n\ell}$  and  $\mathcal{I}_{n\ell}$  are the frequency and inertia of the mode with radial order  $n$  and angular degree  $\ell$ , and  $\mathcal{I}_0(\nu)$  is the mode inertia of the radial modes interpolated at

<sup>4</sup> <https://github.com/warrickball/AADG3>

<sup>5</sup> <https://www.gnu.org/licenses/gpl-3.0.en.html>

**Table 1.** Parameters for linewidths (see eqs 15 and 16).

$x$	$a_x$	$b_x$	$c_x$
$\alpha$	$-3.710 \times 10^0$	$1.073 \times 10^{-3}$	$1.883 \times 10^{-4}$
$\Gamma_\alpha$	$-7.209 \times 10^1$	$1.543 \times 10^{-2}$	$9.101 \times 10^{-4}$
$\Delta\Gamma_{\text{dip}}$	$-2.266 \times 10^{-1}$	$5.083 \times 10^{-5}$	$2.715 \times 10^{-6}$
$\nu_{\text{dip}}$	$-2.190 \times 10^3$	$4.302 \times 10^{-1}$	$8.427 \times 10^{-1}$
$W_{\text{dip}}$	$-5.639 \times 10^{-1}$	$1.138 \times 10^{-4}$	$1.312 \times 10^{-4}$

the frequency  $\nu$ . Because mixed modes have greater inertiae than pure p-modes,  $Q_{n\ell}$  is greater than one, so the mixed modes have narrower linewidths (i.e. they live longer) than the pure p-modes.

### 3.3. Mode amplitudes

To predict the intrinsic mode amplitudes of the stellar oscillations in the power spectrum, we follow the prescription by Chaplin et al. (2011), which is itself based on results by Kjeldsen & Bedding (1995) and Samadi et al. (2007).

We assume that the maximum rms amplitude of the radial modes can be scaled from the solar value by

$$A_{\text{max}}^{\text{rms}} = A_{\text{max},\odot}^{\text{rms}} \beta \left( \frac{L}{L_\odot} \right) \left( \frac{M}{M_\odot} \right)^{-1} \left( \frac{T_{\text{eff}}}{T_{\text{eff},\odot}} \right)^{-2} \quad (18)$$

where  $A_{\text{max},\odot}^{\text{rms}} = 2.1$  ppm in the TESS bandpass and we have taken  $T_{\text{eff},\odot} = 5777$  K. The factor  $\beta$  is defined by

$$\beta = 1 - \exp \left( \frac{T_{\text{eff}} - T_{\text{red}}}{\Delta T} \right) \quad (19)$$

and corrects the formula for the apparent decrease in the amplitudes of the hottest dwarfs. Here,  $\Delta T = 1250$  K and  $T_{\text{red}}$  is the temperature of the red edge of the  $\delta$ -Scuti instability strip at the star's luminosity, which we take as

$$T_{\text{red}} = 8907 \text{ K} \cdot \left( \frac{L}{L_\odot} \right)^{-0.093} \quad (20)$$

For the envelope's full-width half-maximum (FWHM) width  $\Gamma_{\text{env}}$ , we use the scaling relation

$$\Gamma_{\text{env}} = 0.66 \mu\text{Hz} \cdot \left( \frac{\nu_{\text{max}}}{\mu\text{Hz}} \right)^{0.88} \quad (21)$$

If  $T_{\text{eff}} > T_{\text{eff},\odot}$ , we multiply  $\Gamma_{\text{env}}$  by the factor  $1 + 6 \times 10^{-4}(T_{\text{eff}} - T_{\text{eff},\odot})$  (Lund et al., in prep.). The rms power in the mode with radial order  $n$  and angular degree  $\ell$  is then

$$(A_{n\ell}^{\text{rms}})^2 = (A_{\text{max}}^{\text{rms}})^2 \exp \left[ -\frac{(\nu_{n\ell} - \nu_{\text{max}})^2}{2\sigma_{\text{env}}^2} \right] \quad (22)$$

where  $\sigma_{\text{env}} = \Gamma_{\text{env}}/2\sqrt{2\ln 2}$ .

Like the linewidths, the mode powers are also affected by the coupling of p- and g-modes. We divide the mode powers by  $Q_{n\ell}$  (see eq. 17) so that the more strongly coupled modes are suppressed. Finally, to avoid simulating lightcurves for modes that contribute negligibly to the power spectrum, we restrict the list of modes to those with heights in the power spectrum greater than  $10^{-4}$  times the expected granulation background signal.

### 3.4. Background properties and other global variables

To determine the characteristic timescale of the granulation  $\tau_{\text{gran}}$ , we use equation 10 of Kjeldsen & Bedding (2011),

$$\tau_{\text{gran}} = \left( \frac{\nu_{\text{max}}}{\nu_{\text{max},\odot}} \right)^{-1} \tau_{\text{gran},\odot} \quad (23)$$

with a solar value  $\tau_{\text{gran},\odot} = 250$  s. The amplitude of the granulation is given by combining equations 24 and 21 of Kjeldsen & Bedding (2011), which gives

$$\sigma_{\text{gran}} \propto \frac{L^2}{M^3 T_{\text{eff}}^{5.5}} \nu_{\text{max}} \quad (24)$$

The granulation signal drives the oscillations. After it is generated for the mode calculation, it is added to the lightcurve after an appropriate scaling (see Howe et al. 2015).

The amplitude of the white noise is generated according to the same formulae as used in the ATL code. The noise model is inferred from the target's  $I$ -band magnitude, which is similar to the expected magnitude in the TESS bandpass. The white noise is added directly to the lightcurve as Gaussian noise after all other steps of the calculation.

### 3.5. Mode visibilities

The apparent amplitudes of the modes are influenced by two main geometric effects: cancellation and inclination. First, as the angular degree  $\ell$  increases, there are more and more equally-sized brighter and darker regions across the stellar surface, which cancel out when integrated over the visible stellar surface. This cancellation can be quantified by a visibility  $V_\ell$ , often normalised by the radial mode's visibility  $V_0$  to give the normalised visibilities  $\tilde{V}_\ell \equiv V_\ell/V_0$ . The power of a non-radial mode of degree  $\ell$  is then multiplied by  $\tilde{V}_\ell$ .

Though these visibilities can in principle be computed theoretically (e.g. Ballot et al. 2011), Lund et al. (2017) found that the predictions disagreed with observations, especially for the  $\ell = 3$  modes. We have opted to use the median normalised visibilities for the main-sequence stars studied by Lund et al. (2017), which are  $\tilde{V}_1 = 1.505$ ,  $\tilde{V}_2 = 0.62$  and  $\tilde{V}_3 = 0.075$ . We note that Lund

et al. (2017) found no significant correlations with stars' properties and found values in reasonably agreement with the red giants studied by Mosser et al. (2012b).

Second, a rotating star's inclination angle influences the relative visibility of modes of different azimuthal order  $m$ . Assuming equipartition of energy between each of the  $2\ell+1$  components, the power in each  $m$  component is the intrinsic mode power multiplied by a factor (Gizon & Solanki 2003)

$$\mathcal{E}_{\ell m}(i) = \frac{(\ell - |m|)!}{(\ell + |m|)!} \left[ P_{\ell}^{|m|}(\cos i) \right]^2 \quad (25)$$

where  $i$  is the inclination angle of the rotation axis and  $P_{\ell}^{|m|}$  is an associated Legendre polynomial.

We assumed that the rotation axis of each star is randomly distributed over the sphere (i.e. it can point in any direction), which implies that  $\cos i$  is uniformly distributed. We assign the inclination  $i$  for each star by drawing a uniform variate  $w \sim U(0, 1)$  and assigning  $i = \cos^{-1} w$ .

### 3.6. Other parameters

Finally, we summarize our choices for the remaining global parameters in AADG3. As mentioned before, the sequence of driving terms is allowed to relax for 6 d, which, given the 2-minute cadence of the TESS data, corresponds to 4320 data points. The output lightcurves contain 255418 or 257345 points, corresponding to the total length of all the sectors in either the northern or southern ecliptic hemispheres. The full lightcurves are subsequently divided into lightcurves for each sector in which a given star is observed.

## 4. CATALOGUE CONTENTS

### 4.1. Stellar properties and lightcurves

For each star, we simulated a lightcurve for the duration that TESS will observe that hemisphere (roughly 356.2 days) and then separated the lightcurves for each sector in which the star occurs. The lightcurves are publicly available as archives for each sector.<sup>6</sup> The data repository also includes a table of comma-separated values (CSV) containing the data from all of the headers for each lightcurve, for quick analysis of the sample and target selection. We also separately provide all the scripts that were used to produce and manipulate the data.<sup>7</sup> Each lightcurve is a FITS file with a filename of the form

`<ID>_WN_<SECTOR>_<SEC_RANK>.fits`

where

- `<ID>` is the overall rank of the star in the sample, which identifies it uniquely;
- `<SECTOR>` is the sector number, from 1 to 26 (inclusive); and
- `<SEC_RANK>` is the rank assigned by the ATL code for that sector.

So, for example, `00123_WN_17_050.fits` would be the lightcurve for the 123rd star in the sample when observed in the fourth sector in the northern ecliptic hemisphere (the seventeenth sector overall), in which the ATL ranked it 50th for the detectability of its oscillations. The file `00123_WN_18_056.fits` would be a lightcurve for the same star when observed in the fifth sector in the northern ecliptic hemisphere, in which it was ranked 56th for the detectability of its oscillations.

Each file contains a header and two arrays of data, with details of each component given in Table 2. The header contains a number of overall properties of the star, taken from TRILEGAL simulation, the ATL results, the MESA stellar models and the input for AADG3. The first array contains the lightcurve data. The second array contains the mode frequency information used by AADG3 to create the lightcurve. Thus, each lightcurve file contains all the information required to recreate the AADG3 input and the public pipeline repository includes a script to do this.

### 4.2. Example power spectra

#### 4.2.1. Typical low-luminosity red giant

As expected from the ATL and can be seen in Fig. 1, most of the best targets in our sample are found at the base of the red giant branch, with  $T_{\text{eff}} \approx 5000$  K and  $\log g \approx 3.5$ . This is mainly an effect of the relationship between mode amplitude and luminosity. We would in principle prioritise stars further up the red giant branch too but the oscillations of these stars will be available from the full-frame images, with a cadence of 30 minutes. The ATL therefore places a lower limit on  $\nu_{\text{max}}$  of  $240 \mu\text{Hz}$ .

Fig. 3 shows the power spectrum of star 00197, located near the southern ecliptic pole, as observed in sector 2. With  $T_{\text{eff}} = 4933$  K and  $\log g = 3.47$ , this star is typical of the bulk of targets on the lower red giant branch. Fig. 4 shows a power spectrum of the same star but this time computed from the full, roughly year-long lightcurve.

#### 4.2.2. Main-sequence stars

Although the sample is dominated by subgiants and low-luminosity red giants, there are also less evolved

<sup>6</sup> <https://figshare.com/s/3e7afba4fa19e0c2dc1c>

<sup>7</sup> <https://github.com/warrickball/s4tess>



**Table 2.** Detailed contents of the lightcurve FITS files. Each row gives a key’s name, its units (if applicable) and a short description.

Header			Header (cont.)		
Key	Unit	Description	Key	Unit	Description
ID		rank in whole sample	COMP		binarity: 0 if the star is single or 1 or 2 if the star is the primary or secondary in a binary
SECTOR		TESS observing sector	SIGMA	ppm	white noise amplitude
SEC_RANK		rank in this sector	SEED		seed for random number generator
TOT_RANK		rank in whole sky (including stars not observed by TESS)	N_CADS		number of cadences in hemisphere
PMIX		detection probability	GRAN_SIG	ppm	granulation amplitude
MASS	$M_{\odot}$	stellar mass	GRAN_TAU	s	granulation timescale
RADIUS	$R_{\odot}$	stellar radius	INC	$^{\circ}$	inclination angle
AGE	Gyr	stellar age			
TEFF	K	effective temperature	Timeseries array		
LOGG	$\text{cm} \cdot \text{s}^{-2}$	log10 surface gravity	Key	Unit	Description
LUM	$L_{\odot}$	stellar luminosity	TIME	MJD	days since first observation
X_C		central hydrogen abundance	FLUX	ppm	fractional intensity variation
Y_C		central helium abundance	CADENCE_NO		cadences since first observation
Z_INI		initial metal abundance			
FE_H		final metallicity [Fe/H]	Mode data		
OMEGA_C	$\mu\text{Hz}$	central/core rotation rate	Key	Unit	Description
OMEGA_E	$\mu\text{Hz}$	surface/envelope rotation rate	L		angular degree $\ell$
VR	$\text{km} \cdot \text{s}^{-1}$	radial velocity	N		radial order $n$
MUO		distance modulus	FREQ	$\mu\text{Hz}$	frequency
AV		interstellar reddening	WIDTH	$\mu\text{Hz}$	linewidth
ELON	$^{\circ}$	ecliptic longitude	POWER	$\text{ppm}^2$	Rms power
ELAT	$^{\circ}$	ecliptic latitude	ROT	$\mu\text{Hz}$	rotation splitting
GLON	$^{\circ}$	galactic longitude			
GLAT	$^{\circ}$	galactic latitude			
GC		galactic component: 1, 2, 3 or 4 for the thin disc, thick disc, halo or bulge			

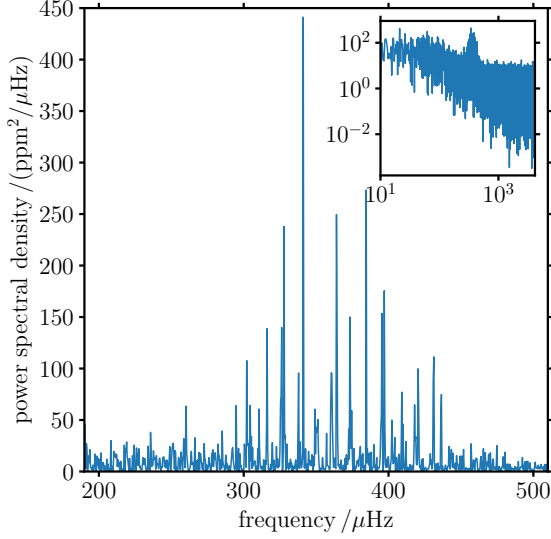
stars. Fig. 5 shows the power spectrum of star 00704, observed in sector 25. This star has similar properties ( $T_{\text{eff}} = 6636 \text{ K}$ ,  $\log g = 4.17$ ) to the known solar-like oscillator KIC 11253226 ( $T_{\text{eff}} = 6642 \text{ K}$ ,  $\log g = 4.18$ ), which Lund et al. (2017) and Silva Aguirre et al. (2017) studied as part of the *Kepler* LEGACY sample.

Fig. 6 shows the power spectrum of star 00771, observed in sector 18. This star is more Sun-like ( $T_{\text{eff}} = 6052 \text{ K}$ ,  $\log g = 4.31$ ) and similar to the *Kepler* targets KIC 6106415 ( $T_{\text{eff}} = 6037 \text{ K}$ ,  $\log g = 4.31$ ) and KIC 6116048 ( $T_{\text{eff}} = 6033 \text{ K}$ ,  $\log g = 4.29$ ), which were also part of the LEGACY sample. Though the  $\ell = 0$  modes are clearly distorted by the  $\ell = 2$  modes, it remains to be seen whether or not the frequencies can be disentangled reliably.

## 5. DISCUSSION

The present simulated results offer reasonably realistic predictions of what the underlying signal from solar-like oscillators observed by TESS will look like. The only source of instrumental noise we have included, however, is the white noise that we have added to the time series. We have not considered other effects that would degrade the power spectra, including instrumental effects or observing gaps. We have also not included other stellar signals like starspots or transits. Any of these, however, can be straightforwardly added to the lightcurves we provide.

A more complicated contaminant is the effect of frequency changes caused by magnetic activity. As the frequencies vary over the course of an observation, so the mode profiles in the power spectrum are broadened and potentially biased (Chaplin et al. 2008a). The effect is probably small in most TESS targets because the



**Figure 3.** Power spectrum of a typical target (star 00197 observed in sector 2) in the range where the oscillations are clearest. The inset shows the complete power spectrum.

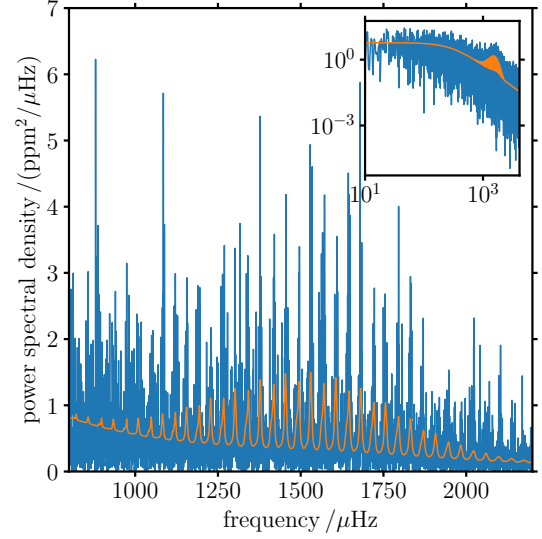


**Figure 5.** Power spectrum for one sector of data of an F-type dwarf, similar to KIC 11253226 (star 00704). The orange line is the mean spectral model with no mode asymmetry. The inset shows the complete power spectrum.

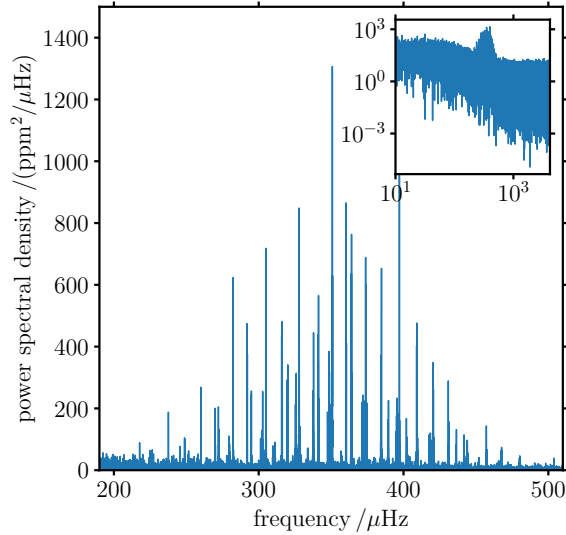


**Figure 4.** Power spectrum of a typical target (star 00197, as in Fig. 3) observed for the maximum duration in the southern hemisphere. The inset shows the complete power spectrum.

roughly month-long observations are much shorter than known activity cycles (e.g. Saikia et al. 2018). AADG3 has inherited the capability of modelling these frequency shifts from earlier versions of the code (Howe et al. 2015) but it has not yet been validated in the new version of the code released with this article. In addition, this would require a further semi-empirical model with which

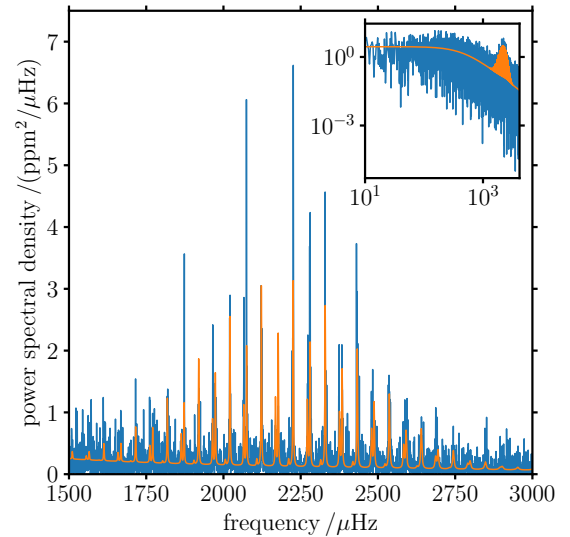


**Figure 6.** Power spectrum for one sector of data of a G-type dwarf, similar to KIC 6106415 and KIC 6116048 (star 00771). The orange line is the mean spectral model with no mode asymmetry. The inset shows the complete power spectrum.

to predict the activity cycle periods and the magnitude of the frequency shifts for each star.

Finally, the code is still limited by our limited ability to predict relevant oscillation parameters, in particular the rotation profiles of the stars. The linewidths (or damping rates) also require an empirical model but at least

they are well constrained by observations from *Kepler*. These are areas of active research and continued asteroseismic analyses will provide important constraints on theoretical models.

Our methods are naturally applicable to any set of time-series observations of solar-like oscillators, be it preparation for upcoming missions like PLATO (Rauer et al. 2014), planning for ongoing projects like the Stellar Oscillations Network Group (SONG, Grundahl et al. 2014) or testing new analyses of existing datasets like *Kepler* or COROT. The PLATO consortium already operates a lightcurve generator, the PLATO Solar-like Light-curve Simulator<sup>8</sup> (PSLS), which is based on the COROT simulator (*simuLC*, Baudin et al. 2007). The PLATO and COROT simulators produce an oscillation lightcurve by the inverse Fourier transform of a model Fourier spectrum and our method (which works entirely in the time-domain) is complementary.

## 6. CONCLUSIONS

We have presented a catalogue of mock observations of solar-like oscillators observed by NASA’s TESS mission in its short-cadence mode. Our artificial data combines a simulation of Milky Way populations, detailed stellar models and empirical relations for less well understood physical processes. Targets have been selected from the galaxy simulation using the same method as has been used for the actual mission and the sample therefore reflects the same selection effects. Together, these provide realistic lightcurves with which to prepare for the steady stream of data expected from TESS.

Our artificial lightcurves are publicly available<sup>9</sup> and can be extended to include various phenomena that we have excluded, be they instrumental effects or other astrophysical signals. The methods we have presented are also applicable to any observing programme for solar-like oscillations and will be useful in the future for observatories like SONG and PLATO.

WHB would like to thank Tom Barclay for providing detailed help with and information about TESS’s orbit and pointings. AM acknowledges support from the European Research Council (ERC) under the European Union’s Horizon 2020 research and innovation programme (project ASTEROCHRONOMETRY, grant agreement no. 772293). The authors thank the UK Science and Technology Facilities Council (STFC) for support under grant ST/R0023297/1. AM, GRD, and LG are grateful to the International Space Science Institute (ISSI) for support provided to the asteroSTEP ISSI International Team. Calculations in this paper made use of the University of Birmingham’s BlueBEAR High-Performance Computing service.<sup>10</sup> Previous development of AADG3 has been supported by the International Space Science Institute (ISSI), through a workshop programme award, and by the European Helio- and Asteroseismology Network (HELAS), a major international collaboration funded by the European Commissions Sixth Framework Programme.

*Software:* NumPy<sup>11</sup>, SciPy<sup>12</sup>, Astropy<sup>13</sup> (Astropy Collaboration et al. 2013), Matplotlib<sup>14</sup> (Hunter 2007)

## REFERENCES

- Aarslev, M. J., Houdek, G., Handberg, R., & Christensen-Dalsgaard, J. 2018, MNRAS, 478, 69
- Angus, R., Aigrain, S., Foreman-Mackey, D., & McQuillan, A. 2015, MNRAS, 450, 1787
- Appourchaux, T., Antia, H. M., Benomar, O., et al. 2014, A&A, 566, A20
- Astropy Collaboration, Robitaille, T. P., Tollerud, E. J., et al. 2013, A&A, 558, A33
- Auvergne, M., Bodin, P., Boissard, L., et al. 2009, A&A, 506, 411
- Ball, W. H., Beeck, B., Cameron, R. H., & Gizon, L. 2016, A&A, 592, A159
- Ball, W. H., & Gizon, L. 2014, A&A, 568, A123
- Ballot, J., Barban, C., & van’t Veer-Menneret, C. 2011, A&A, 531, A124
- Basu, S., & Chaplin, W. J. 2017, Asteroseismic Data Analysis: Foundations and Techniques, Princeton Series in Modern Observational Astronomy (Princeton Univ. Press, Princeton, NJ)
- Baudin, F., Samadi, R., Appourchaux, T., & Michel, E. 2007, in The CoRoT Book, ed. F. Favata, A. Baglin, L. Conroy, & J. Lochard (ESA Publications Division)
- Benomar, O., Takata, M., Shibahashi, H., Ceillier, T., & García, R. A. 2015, MNRAS, 452, 2654
- Borucki, W. J., Koch, D., Basri, G., et al. 2010, Science, 327, 977
- <sup>8</sup> <https://sites.lesia.obspm.fr/psls/>
- <sup>9</sup> <https://figshare.com/s/3e7afba4fa19e0c2dc1c>
- <sup>10</sup> <http://www.birmingham.ac.uk/bear>
- <sup>11</sup> <http://www.numpy.org>
- <sup>12</sup> <http://www.scipy.org>
- <sup>13</sup> <http://www.astropy.org>
- <sup>14</sup> <http://matplotlib.org>

- Campante, T. L., Schofield, M., Kuszlewicz, J. S., et al. 2016, *ApJ*, 830, 138
- Chaplin, W. J., Elsworth, Y., Howe, R., et al. 1997, *MNRAS*, 287, 51
- Chaplin, W. J., Elsworth, Y., New, R., & Toutain, T. 2008a, *MNRAS*, 384, 1668
- Chaplin, W. J., Appourchaux, T., Baudin, F., et al. 2006, *MNRAS*, 369, 985
- Chaplin, W. J., Appourchaux, T., Arentoft, T., et al. 2008b, *Astronomische Nachrichten*, 329, 549
- Chaplin, W. J., Kjeldsen, H., Bedding, T. R., et al. 2011, *ApJ*, 732, 54
- Christensen-Dalsgaard, J. 2008, *Ap&SS*, 316, 113
- Davies, G. R., Handberg, R., Miglio, A., et al. 2014, *MNRAS*, 445, L94
- Deheuvels, S., Doğan, G., Goupil, M. J., et al. 2014, *A&A*, 564, A27
- Dichmann, D., Parker, J., Nickel, C., & Lutz, S. 2016, in *AIAA/AAS Astrodynamics Specialist Conference*, AIAA SPACE Forum, (AIAA 2016-5664)
- Dichmann, D., Parker, J., Williams, T., & Mendelsohn, C. 2014, in *24th International Symposium on Space Flight Dynamics*
- Dupret, M.-A., Grigahcène, A., Garrido, R., Gabriel, M., & Scuflaire, R. 2004, *A&A*, 414, L17
- Eggenberger, P., Montalbán, J., & Miglio, A. 2012, *A&A*, 544, L4
- Ferguson, J. W., Alexander, D. R., Allard, F., et al. 2005, *ApJ*, 623, 585
- Girardi, L., Groenewegen, M. A. T., Hatziminaoglou, E., & da Costa, L. 2005, *A&A*, 436, 895
- Girardi, L., Barbieri, M., Groenewegen, M. A. T., et al. 2012, *Astrophysics and Space Science Proceedings*, 26, 165
- Gizon, L., & Solanki, S. K. 2003, *ApJ*, 589, 1009
- Grevesse, N., & Noels, A. 1993, in *Origin and Evolution of the Elements*, ed. N. Prantzos, E. Vangioni-Flam, & M. Casse, 15–25
- Grundahl, F., Christensen-Dalsgaard, J., Pallé, P. L., et al. 2014, in *IAU Symposium*, Vol. 301, *IAU Symposium*, ed. J. A. Guzik, W. J. Chaplin, G. Handler, & A. Pigulski, 69–75
- Houdek, G. 2017, in *European Physical Journal Web of Conferences*, Vol. 160, *European Physical Journal Web of Conferences*, 02003
- Houdek, G., Trampedach, R., Aarslev, M. J., & Christensen-Dalsgaard, J. 2017, *MNRAS*, 464, L124
- Howe, R. 2009, *Living Reviews in Solar Physics*, 6, 1
- Howe, R., Davies, G. R., Chaplin, W. J., Elsworth, Y. P., & Hale, S. J. 2015, *MNRAS*, 454, 4120
- Howell, S. B., Sobeck, C., Haas, M., et al. 2014, *PASP*, 126, 398
- Hunter, J. D. 2007, *Computing In Science & Engineering*, 9, 90
- Iglesias, C. A., & Rogers, F. J. 1996, *ApJ*, 464, 943
- Jiménez-Reyes, S. J., Chaplin, W. J., García, R. A., et al. 2008, *MNRAS*, 389, 1780
- Jørgensen, A. C. S., Weiss, A., Mosumgaard, J. R., Silva Aguirre, V., & Sahlholdt, C. L. 2017, *MNRAS*, 472, 3264
- Katz, D., Sartoretti, P., Cropper, M., et al. 2018, *ArXiv e-prints*, arXiv:1804.09372
- Kjeldsen, H., & Bedding, T. R. 1995, *A&A*, 293, 87
- . 2011, *A&A*, 529, L8
- Kjeldsen, H., Bedding, T. R., & Christensen-Dalsgaard, J. 2008, *ApJL*, 683, L175
- Krishna Swamy, K. S. 1966, *ApJ*, 145, 174
- Lund, M. N., Silva Aguirre, V., Davies, G. R., et al. 2017, *ApJ*, 835, 172
- Marques, J. P., Goupil, M. J., Lebreton, Y., et al. 2013, *A&A*, 549, A74
- Mosser, B., Goupil, M. J., Belkacem, K., & et al. 2012a, *A&A*, 548, A10
- Mosser, B., Elsworth, Y., Hekker, S., et al. 2012b, *A&A*, 537, A30
- Nielsen, M. B., Schunker, H., Gizon, L., & Ball, W. H. 2015, *A&A*, 582, A10
- Nielsen, M. B., Schunker, H., Gizon, L., Schou, J., & Ball, W. H. 2017, *A&A*, 603, A6
- Paxton, B., Bildsten, L., Dotter, A., et al. 2011, *ApJS*, 192, 3
- Paxton, B., Cantiello, M., Arras, P., et al. 2013, *ApJS*, 208, 4
- Rauer, H., Catala, C., Aerts, C., et al. 2014, *Experimental Astronomy*, 38, 249
- Ricker, G. R., Winn, J. N., Vanderspek, R., et al. 2015, *Journal of Astronomical Telescopes, Instruments, and Systems*, 1, 014003
- Rodrigues, T. S., Bossini, D., Miglio, A., et al. 2017, *MNRAS*, 467, 1433
- Rogers, F. J., & Nayfonov, A. 2002, *ApJ*, 576, 1064
- Saikia, S. B., Marvin, C. J., Jeffers, S. V., et al. 2018, *A&A*, 616, A108
- Samadi, R., Georgobiani, D., Trampedach, R., et al. 2007, *A&A*, 463, 297
- Schlegel, D. J., Finkbeiner, D. P., & Davis, M. 1998, *ApJ*, 500, 525
- Silva Aguirre, V., Lund, M., Antia, H. M., et al. 2017, *ApJ*, 835, 173
- Sonoi, T., Belkacem, K., Dupret, M.-A., et al. 2017, *A&A*, 600, A31
- Sonoi, T., Samadi, R., Belkacem, K., et al. 2015, *A&A*, 583, A112



- Sullivan, P. W., Winn, J. N., Berta-Thompson, Z. K., et al. 2015, *ApJ*, 809, 77
- Torres, G. 2010, *AJ*, 140, 1158
- Toutain, T., Elsworth, Y., & Chaplin, W. J. 2006, *MNRAS*, 371, 1731
- Townsend, R. H. D., Goldstein, J., & Zweibel, E. G. 2018, *MNRAS*, 475, 879
- Townsend, R. H. D., & Teitler, S. A. 2013, *MNRAS*, 435, 3406
- Trampedach, R., Aarslev, M. J., Houdek, G., et al. 2017, *MNRAS*, 466, L43
- Turck-Chièze, S., Palacios, A., Marques, J. P., & Nghiem, P. A. P. 2010, *ApJ*, 715, 1539